International Journal of Computational Methods and Experimental Measurements
https://www.acadlore.com/journals/IJCMEM

Joule Heating and Viscosity-Ratio Effects on Dissipative Ternary Nanofluid Flow over a Permeable Surface

Sudha Mahanthesh Sachhin[1], Kenchappa Nagegowda[1], Ulavathi Shettar Mahabaleshwar[1], Laura Milena Pérez[2], Giulio Lorenzini[3*]

[1] Department of Studies in Mathematics, Davangere University, 577007 Davangere, India
[2] Department of Industrial and Systems Engineering, University of Tarapacá, 1000000 Arica, Chile
[3] Department of Industrial Systems and Technologies Engineering, University of Parma, 43124 Parma, Italy

* Correspondence: Giulio Lorenzini (giulio.lorenzini@unipr.it)

Received: 01-15-2026 **Revised:** 02-27-2026 **Accepted:** 03-17-2026

Citation: S. M. Sachhin, K. Nagegowda, U. S. Mahabaleshwar, L. M. Pérez, and G. Lorenzini, "Joule heating and viscosity-ratio effects on dissipative ternary nanofluid flow over a permeable surface," *Int. J. Comput. Methods Exp. Meas.*, vol. 14, no. 1, pp. 57–80, 2026. https://doi.org/10.56578/ijcmem140104.

© 2026 by the author(s). Licensee Acadlore Publishing Services Limited, Hong Kong. This article can be downloaded for free, and reused and quoted with a citation of the original published version, under the CC BY 4.0 license.

Abstract: This study examines the effects of viscous dissipation, Joule heating, and coupled heat transfer on dissipative ternary nanofluid flow over a permeable surface. The ternary nanofluid is composed of Al_2O_3, SiO_2, and TiO_2 nanoparticles dispersed in water as the base fluid. By introducing suitable similarity transformations, the governing partial differential equations are reduced to a coupled system of ordinary differential equations. The thermal field is analyzed for both prescribed surface temperature (PST) and prescribed heat flux (PHF) conditions, while a temperature-dependent heat source/sink term is incorporated to maintain energy balance within the fluid domain. The resulting energy equation is treated analytically with the aid of Kummer's function and Laguerre polynomial techniques. The effects of the main controlling parameters, including the inverse Darcy number, magnetic parameter, viscosity-ratio parameter, and radiation parameter, are discussed with the support of graphical results. It is found that an increase in the magnetic parameter reduces the velocity by about 12% and raises the temperature by nearly 18%. These findings provide useful guidance for the design and thermal optimization of engineering systems involving complex nanofluids in porous media, including polymer extrusion and automotive cooling applications.

Keywords: Porous medium; Thermal radiation; Viscosity ratio; Joule heating; Inclined magnetic field; Viscous dissipation

1 Introduction

Magnetic fields influence the movement of fluids in numerous industrial applications, where they serve as a novel, non-invasive tool to direct and control the flow of liquids. A typical example is the water treatment sector, where magnetic flow meters are chosen for their high accuracy in gauging the flow rate of water and wastewater. This is a pivotal technology for the management and distribution of water resources. Food and beverage industries rely on these meters to help maintain standard product quality by precisely measuring the flow of liquid ingredients. Likewise, the pharmaceutical industry turns to the accuracy of magnetic flow meters to carry out hygienic and exact measurements of sensitive fluids that are not in direct contact. These fluids allow for the adjustment of resistance and damping in different scenarios, thus improving the performance and safety of vehicles and machines. The scope of magnetic applications in fluid dynamics underlines their indispensable function in the evolution of industrial operations and product quality. Due to many applications, many authors examined magnetic flow, such as Dolui et al. [1], who examined the importance of ternary nanoparticle flow, particularly on the interactions at the Hiemenz stagnation point and the influence of a magnetic field on the flow behaviour as it moves over a surface. Turkyilmazoglu [2] explored the dynamics of porous media with heat transfer. Jan et al. [3] and Mishra et al. [4] studied the magnetohydrodynamics (MHD) 2-D ternary nanofluid flow based on polymers with different thermal conductivity and partial slip. The influences of the MHD and Cattaneo-Christov models on a Maxwell fluid stagnation-point movement are explored by Chen et al. [5].

The viscosity ratio plays a major role in various industrial and real-world applications. It is instrumental in the examination of fluid flow through porous media, which is a common scenario in sectors such as chemical engineering,

environmental analysis, and biomedical engineering. For instance, in chemical engineering, the viscosity ratio is used to optimize the design of filtration mechanisms, ensuring efficient separation processes. In environmental implications, many researchers explored the viscosity ratio, such as Pavlov [6], who studied the two-dimensional MHD fluid movement. Zhang et al. [7] examined the electro-MHD characteristic in non-Newtonian fluids, particularly of the third grade, involving interactions between the fluid's inherent characteristics and the external electric and magnetic fields. The Gauss-Seidel iteration method and quasi-linearization are used by Yao et al. [8] and Murali et al. [9] to study the 3-D Darcy-Brinkman-Forchheimer flow terms. The Brinkman impact on fluid flow was studied by Tso and Mahulikar [10] and Bèg et al. [11] by using numerical findings produced by a robust double-shot Runge-Kutta-Merson scheme and a finite-difference approach. Moreover, the viscosity ratio's relevance extends to the biomedical sphere, particularly in drug delivery systems, where understanding fluid flow at the microscale can enhance the precision of targeted therapies. The adaptability of the viscosity ratio model to Newtonian and non-Newtonian fluids makes it a versatile method for researchers and engineers, allowing for precise predictions and improvements in fluid flow systems over a broad spectrum of applications.

Joule heating is used to keep precise temperatures in reactors and distillation columns, which is necessary for the uniformity and quality of the products. The plastics industry benefits from this effect in operations such as injection moulding and extrusion to adjust the viscosity of the material so that it flows easily and is shaped accurately. In the food and beverage industry, Joule heating is used for distillation, drying, cooking, etc., where consistent and uniform heat distribution is the key. Because of numerous applications, a number of researchers have studied Joule heating, such as Nayak et al. [12], who explored the MHD nano liquid flow via a permeable linear stretching surface with convective heating and a porous matrix. Leng et al. [13] and Kaingu et al. [14] explored the consequences of suction/injection and MHD Casson nanofluid flow for a nonlinearly expanding surface. Nazeer et al. [15] explored the Newtonian liquids Walters-B liquid transport mass and energy when they enter the flow via a penetrable surface that is semi-infinite. Khan et al. [16] researched the MHD fluid flow over a linear stretching surface with convective heating in the presence of a porous medium. Furthermore, in microfluidics, the heat generated by the Joule effect is used to open microvalves by the thermal expansion of the parts, thus showing its dual capability in both large-scale operations and small, highly precise applications.

Porous media is playing a main role in the direction and control of fluid flow in different industrial and real-world applications. The materials, which are permeable by nature, are allowing the controlled movement and spreading of fluids; porous media are very important in extraction processes. For example, it is essential to understand the multiphase flow within porous rocks for the efficient recovery of oil. Similarly, in environmental engineering, the study of fluid flow through soil and rock is fundamental for groundwater management and contamination mitigation. Sachhin et al. [17] studied the slanted magnetic field that affects fluid flow across a permeable, shrinking surface while allowing for heat transmission. Patnaik et al. [18] and Bég et al. [19] explored the convective boundary layer movement of a nanofluid via an extending sheet in a porous medium under unstable MHD conditions. A nanoparticle-enhanced porous medium embedded on a vertical flat surface with a steady mixed convection flow is investigated by Waini [20]. Joshi et al. [21] and Wang et al. [22] have examined the effects of heat radiation along with different viscosities on the flow of nanofluid over a rotating disk with permeable media. The development of microfluidic model porous media has made it possible to see and understand the complex fluid dynamics at the pore level, which has resulted in better designs and processes in industries such as food and wood production. Furthermore, the combination of data-driven methods and physics-informed machine learning is changing the traditional modeling and prediction of these flows, thus giving new insights and optimization strategies for these vital systems.

Thermal radiation fundamentally affects the communication of heat and thus energy transfer efficiency in fluid flows through industrial processes. From a thermal engineering perspective, figuring out how thermal radiation affects fluid flow is a must if one is to optimize industrial processes. For instance, the chemical industry uses radiation to keep reactors or distillation columns at the right temperature so the reaction is just efficient and the product quality is good. Likewise, in plastic industries, temperature control through radiation during injection molding and extrusion can help in obtaining the desired properties of materials. The food and beverage industry also uses radiation to provide the required heat in processes like distillation, drying, and cooking. Due to many applications, many researchers examined the radiation, such as Sachhin et al. [23], who explored how a slanted MHD influences fluid movement over an expanding/shrinking sheet while allowing for heat transmission. Yu and Wang [24] and Li et al. [25] explored the flow and temperature between two extending, spinning disks within a water flow. Bejawada and Nandeppanavar [26], Hosseinzadeh et al. [27], and Megahed [28] studied the micropolar liquid flow across a vertical permeable plate. Also, in high-temperature environments such as nuclear reactors or electronic cooling systems, thermal radiation helps to control heat transfer; thus, the safety and the life span of the equipment are improved. Incorporating the concepts of thermal radiation in fluid flow systems results in improvements in energy conservation and process efficiency, thereby highlighting its importance in industrial applications as well as in everyday life. Viscosity dissipation is taken into consideration by Ragueb and Mansouri [29] to study the laminar heat transfer inside a cross-section duct that is exposed to a uniform wall temperature. Schranner et al. [30] and

Lelea and Cioabla [31] study the problem of heat transmission and the flow of incompressible fluid movements across various boundaries. Bataller [32], Tso et al. [33], and Megahed [28] study the viscous dissipation effects. Dadheech et al. [34], Crane [35], and Hamid et al. [36] study the heat transfer in stretching surfaces. Xiang et al. [37], Shanmugam and Maganti [38], and Agravat et al. [39] study the heat source/sink performance. Ullah et al. [40] and Flity et al. [41] study the effect of thermal conductivity on fluid flow. Bognár [42], Lone et al. [43], and Barna et al. [44] develop similarity solutions and analytical approaches for non-Newtonian and boundary layer flows. Klazly and Bognár [45] and Bognár and Hriczó [46] investigate empirical modeling of nanofluid properties and ferrofluid flow under magnetic effects. Usafzai et al. [47] comprehensively studies nanofluid and hybrid nanofluid transport phenomena over stretching and permeable surfaces.

Mahabaleshwar et al. [48–50] analyze porous media flow, convection, and magnetohydrodynamic effects in complex fluids. Khan et al. [51], Hatami and Ganji [52], Jenifer and Saikrishnan [53], Sachhin et al. [54], and Hamid et al. [36] present advanced studies on entropy generation and thermal transport mechanisms.

1.1 Physical Application Scenario

The present model is motivated by the thermal management of high-heat-flux electronic devices mounted on porous substrates, such as microprocessors, power electronics modules, and compact heat exchangers. In these systems, electrically conducting ternary nanofluids are circulated through porous heat sinks to enhance cooling performance. The presence of an external magnetic field enables control of the fluid motion, making MHD effects essential for accurate prediction. Since the coolant flows through porous structures (e.g., metal foams), the Darcy–Brinkman formulation is required to account for both permeability resistance and viscous diffusion within the medium. The electrical conductivity of the nanofluid leads to Joule heating under magnetic fields, while high shear near stretching surfaces produces viscous dissipation. At elevated temperatures, thermal radiation further contributes to heat transfer, necessitating the simultaneous inclusion of all these mechanisms.

The two thermal boundary conditions considered also reflect practical operating modes. The prescribed surface temperature (PST) condition represents actively temperature-controlled systems where the wall temperature is maintained constant, whereas the prescribed heat flux (PHF) condition corresponds to devices operating at fixed power dissipation, where the surface temperature adjusts according to the heat removal rate. Thus, the present formulation provides a realistic theoretical framework for magnetically controlled cooling of porous electronic systems using advanced ternary nanofluids.

1.2 Motivation and Novelty

The motivation of the present study comes from the real-life applications of thermal management and materials processing systems where electrically conducting nanofluids are made to flow over porous and permeable surfaces while being subjected to external magnetic fields. For instance, one may think of cooling the electronic components, which are mounted on porous substrates, using magnetic fields, or the polymer extrusion over porous molds that are electrically heated, or the energy systems where the nanoparticle-enhanced coolants are circulated through the magnetized porous heat exchangers. In such scenarios, the coexistence of strong magnetic fields and electrically conducting hybrid ternary nanofluids leads to the generation of Joule heating, while the viscous dissipation, caused by the high shear rates in the vicinity of stretching or shrinking surfaces, results in thermal changes that are of significant magnitude. Besides that, at high operating temperatures, radiation heat transfer cannot be disregarded, especially in porous media where the radiative heat flux can combine with the conduction and convection mechanisms.

The porous medium model is used to describe the scenario accurately by including the contribution of viscous and permeability effects, which are inseparable in a porous structure and cannot be explained with the classical Darcy formulation, which refers only to the permeability effect. The choice of both surface temperature (PST) and heat flux (PHF) boundary conditions is made to indicate that, in practice, there exist two types of thermal control strategies, and both are to some extent standard industrial procedures, depending on whether it is surface temperature or heat input that gets regulated. Ignoring any of these mechanisms may cause one not to have a complete picture of the underlying physics and, in turn, may lead to the wrong evaluation of velocity, temperature, skin friction, and heat transfer rates. Therefore, the present work offers a consistent and physically reliable theoretical basis that integrates the co-action of hybrid ternary nanofluids, MHD, porous media, Joule heating, viscous dissipation, and thermal radiation into a single problem.

2 Mathematical Analysis and Solution

2.1 Modeling Assumptions and Boundary Layer Formulation

The current mathematical setup relies on several assumptions about physical phenomena. Figure 1 shows the physical representation of the problem. The flow is assumed steady, 2D, laminar, and incompressible. The nanofluid base with ternary nanoparticles uniformly distributed was treated as a single-phase medium with modified thermophysical properties. The porous medium is homogeneous and isotropic, and the porous medium's effect is

introduced by the Darcy-Brinkman model that allows for both permeability resistance and viscous diffusion effects. Thus, the magnetic field is tilted. Hall and ion-slip effects are not taken into account. The electrical conductivity of the fluid is considered constant. The pressure gradient along the surface is neglected, and body forces other than the Lorentz force are not taken into consideration. In the energy equation, viscous dissipation and Joule heating are kept since they are significant in high-shear and electrically conducting flows. Thermal radiation is accounted for by using the Rosseland diffusion approximation, which is suitable for optically thick media where the radiative heat flux acts like a diffusive process. Higher-degree temperature terms in the expansion of the radiative heat flux are discarded for the sake of mathematical convenience while still keeping the leading radiative part.

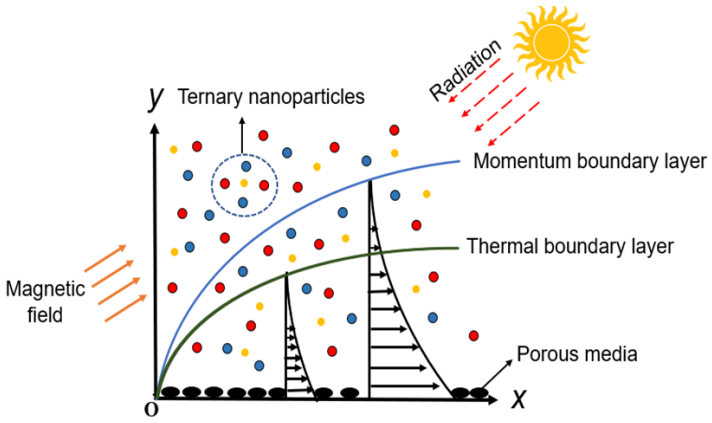


Figure 1. Physical representation of the problem

Governing equations [1, 8, 12, 24]:

$$\frac{\partial u}{\partial x}+\frac{\partial v}{\partial y}=0 \tag{1}$$

$$u\frac{\partial u}{\partial x}+v\frac{\partial u}{\partial y}=\frac{\mu_{eff}}{\rho_{tnf}}\frac{\partial^2 u}{\partial y^2}-\frac{\sigma_{tnf}}{\rho_{tnf}}{B_0}^2 u\,\mathrm{Sin}^2(\tau)-\frac{\mu_{tnf}}{\rho_{tnf}K*}u \tag{2}$$

$$u\frac{\partial T}{\partial x}+v\frac{\partial T}{\partial y}=\frac{1}{(\rho C_p)_{tnf}}\left[\kappa_{tnf}\frac{\partial^2 T}{\partial y^2}-\frac{\partial q_r}{\partial y}+Q_0\left(T-T_\infty\right)+\mu_{tnf}\left(\frac{\partial u}{\partial y}\right)^2+\sigma_{tnf}{B_0}^2u^2\,\mathrm{Sin}^2(\tau)\right] \tag{3}$$

Boundary conditions are given as [2, 6, 17]:

$$\begin{array}{llll} u=cx+A\frac{\partial u}{\partial y}+B\frac{\partial^2 u}{\partial y^2}, & v=v_w, & \text{at} & y=0 \\ u=0, & v=0, & \text{as} & y\to\infty \end{array} \tag{4}$$

PST and PHF case boundary conditions (B. Cs) are:

$$T=T_w=T_\infty+b\left(\frac{x}{l}\right)^2 \text{at} y=0, T\to T_\infty, \text{as} y\to\infty, \tag{5}$$

$$-\kappa\frac{\partial T}{\partial y}=q_w=D\left(\frac{x}{l}\right)^2 \text{at} y=0, T\to T_\infty, \text{as} y\to\infty. \tag{6}$$

where, D denotes a mass flux term, S is the mass transpiration at the plate, b and l terms are constants.

Thermal radiative heat flux estimated by Rosseland's approximation is written as [2, 6, 17]:

$$q_r=-\frac{4\sigma^*}{3k^*}\frac{\partial T^4}{\partial y} \tag{7}$$

where, σ^* is the Stephen Boltzmann constant and k^* is the absorption parameter.

By using the Taylor series and solving T^4 and ignoring the upper-order terms to get:

$$T^4\cong 4{T_\infty}^3T-3{T_\infty}^4 \tag{8}$$

Hence, Eq. (3) becomes:

$$u\frac{\partial T}{\partial x}+v\frac{\partial T}{\partial y}=\frac{1}{(\rho C_p)_{tnf}}\left[\begin{array}{l}\left(\kappa_{tnf}+\frac{16\sigma^* T_\infty^3}{3k^*}\right)\frac{\partial^2 T}{\partial y^2}+Q_0\left(T-T_\infty\right)+\mu_{tnf}\left(\frac{\partial u}{\partial y}\right)^2\\ +\sigma_{tnf}B_0^2u^2\,\mathrm{Sin}^2(\tau)\end{array}\right] \tag{9}$$

Similarity conversions are given as [2, 6, 17]:

$$\psi\left(\eta\right)=x\sqrt{a\,\nu_f}\;f\left(\eta\right),\quad T\left(\eta\right)=T_\infty+\Delta T\theta\left(\eta\right),\quad \eta=y\sqrt{\frac{a}{\nu_f}} \tag{10}$$

$$u=\frac{\partial\psi}{\partial y}=axf'(\eta), v=-\frac{\partial\psi}{\partial x}=-\sqrt{av_f}f(\eta) \tag{11}$$

Given the considerations above, the original system of PDEs in the description of the process is simplified to the standard boundary layer equations that allow similarity transformations to be carried out, thus obtaining the system of nonlinear ordinary differential equations (ODEs) in Eqs. (12)–(18):

$$\Lambda f'''+A_2\left(f\,f''-f'^2\right)-A_3M\mathrm{Sin}^2\left(\tau\right)f'-A_1Da^{-1}f'=0 \tag{12}$$

PST case:

$$\frac{1}{\mathrm{Pr}}\left(A_4+Nr\right)\theta''+A_5\left(f\theta'-2f'\theta\right)+Ni\,\theta+Ec_1\left[A_1f''^2+A_3M\mathrm{Sin}^2\left(\tau\right)f'^2\right]=0 \tag{13}$$

PHF case:

$$\frac{1}{\mathrm{Pr}}\left(A_4+Nr\right)\varphi''+A_5\left(f\varphi'-2f'\varphi\right)+Ni\,\varphi+Ec_2\left[A_1f''^2+A_3M\mathrm{Sin}^2\left(\tau\right)f'^2\right]=0 \tag{14}$$

Modified B. Cs are obtained as:

$$\begin{array}{rl}f(0)=S,\quad f'(0)=d+\xi_1f''(0)+\xi_2f'''(0),\text{ at}\quad \eta\to 0,\\ f'(\eta)\to 0,\text{ as}\quad \eta\to\infty.\end{array} \tag{15}$$

PST case:

$$\theta\left(0\right)=1,\text{at}\eta=0,\text{and}\theta\to\infty,\text{as}\eta\to\infty \tag{16}$$

PHF case:

$$\varphi'\left(0\right)=-1\text{at}\eta=0,\text{and}\varphi\to\infty,\text{as}\eta\to\infty \tag{17}$$

$$A_1=\frac{\mu_{tnf}}{\mu_f},\;A_2=\frac{\rho_{tnf}}{\rho_f},\;A_3=\frac{\sigma_{tnf}}{\sigma_f},\;A_4=\frac{\kappa_{tnf}}{\kappa_f},\;A_5=\frac{(\rho C_p)_{tnf}}{(\rho C_p)_f} \tag{18}$$

The governing nondimensional terms utilized in Eqs. (12) to (18) can be stated as:$M\left(=\frac{\sigma_f{B_0}^2}{a\rho_f}\right)$ is the magnetic field, $\mathrm{Pr}\left(=\frac{\mu_f(C_p)_f}{\kappa_f}\right)$ is Prandtl number, $Nr\left(=\frac{16\sigma^*{T_\infty}^3}{3\kappa_fk^*}\right)$ is thermal radiation, $Ni\left(=\frac{Q_0}{a(\rho C_p)_f}\right)$ represents heat source.

Now, C_f and Nu is calculated by:

$$C_f=\frac{\tau_w}{\rho_f{u_w}^2},Nu=\frac{xq_w}{\kappa\left(T_w-T_\infty\right)} \tag{19}$$

where,

$$\tau_w=-\mu_{eff}\left(\frac{\partial u}{\partial y}\right)_{y=0} \tag{20}$$

$$q_w=-\kappa_{tnf}\left(\frac{\partial T}{\partial y}\right)_{y=0}+\left(q_r\right)_w \tag{21}$$

Skin friction and Nusselt numbers as:

$$C_f\sqrt{\mathrm{Re}_x}=-\Lambda f''\left(0\right) \tag{22}$$

$$\frac{Nu}{\sqrt{\mathrm{Re}_x}}=-\left(A_4+Nr\right)\theta'\left(0\right) \tag{23}$$

where, $\mathrm{Re}_x=\frac{a\,x^2}{\nu_f}$ is the local Reynolds number.

2.2 Analytic Solution for Momentum Equation

By the B. Cs the solution obtained as:

$$f(\eta) = D_1 + D_2\, e^{-\beta\eta} \tag{24}$$

where, $\beta > 0$ and:

$$D_1 = S - D_2, D_2 = \frac{d}{\xi_2\beta^3 - \xi_1\beta^2 - \beta} \tag{25}$$

Put Eqs. (24) and (25) in Eq. (12), then we get the following equation:

$$E_1\beta^4 + E_2\beta^3 + E_3\beta^2 + E_4\beta + E_5 = 0 \tag{26}$$

The roots of Eq. (26) are as:

$$\beta = -\frac{E_2}{4E_1} \pm \frac{1}{2}\sqrt{\left[\frac{E_2^2}{4E_1^2} - \frac{2E_3}{3E_1} + \frac{2^{1/3}\Delta_1}{3E_1\left(\Delta_2 + \sqrt{-4\Delta_1^3 + \Delta_2^2}\right)^{1/3}} + \frac{\left(\Delta_2 + \sqrt{-4\Delta_1^3 + \Delta_2^2}\right)^{1/3}}{3\times 2^{1/3}E_1}\right]} \pm \frac{1}{2}\sqrt{\left[\frac{\frac{E_2^2}{2E_1^2} - \frac{4E_3}{3E_1} - \frac{2^{1/3}\Delta_1}{3E_1\left(\Delta_2+\sqrt{-4\Delta_1^3+\Delta_2^2}\right)^{1/3}} - \frac{\left(\Delta_2+\sqrt{-4\Delta_1^3+\Delta_2^2}\right)^{1/3}}{3\times 2^{1/3}E_1}\frac{E_2^3}{E_1^3} + \frac{4E_2E_3}{E_1^2} - \frac{8E_4}{E_1}}{4\left[\frac{E_2^2}{2E_1^2} - \frac{2E_3}{3E_1} + \frac{2^{1/3}\Delta_1}{3E_1\left(\Delta_2+\sqrt{-4\Delta_1^3+\Delta_2^2}\right)^{1/3}} + \frac{\left(\Delta_2+\sqrt{-4\Delta_1^3+\Delta_2^2}\right)^{1/3}}{3\times 2^{1/3}E_1}\right]}\right]} \tag{27}$$

where,

$$E_1 = \Lambda\xi_2, E_2 = \left(A_2S\xi_2 - \Lambda\xi_1\right), E_3 = \left(A_2S\xi_1 - \xi_2A_1Da^{-1} - A_3M\,\mathrm{Sin}^2(\tau)\xi_2\right),$$
$$E_4 = \left(A_2S + A_3M\,\mathrm{Sin}^2(\tau)\xi_1 + \xi_1A_1Da^{-1}\right) E_5 = A_2d + A_3M\,\mathrm{Sin}^2(\tau) + A_1Da^{-1}$$
$$\Delta_1 = E_3^2 - 3E_2E_4 + 12E_1E_5, \Delta_2 = 2E_3^2 - 9E_2E_3E_4 + 27E_1E_4^2 + E_2^2E_5 - 72E_1E_3E_5$$

Reduced skin friction coefficient can be evaluated by:

$$f'(\eta) = \frac{d}{1 + \xi_1\beta - \xi_2\beta^2}\, e^{-\beta\eta} \tag{28}$$

2.3 Analytic Solution for the Energy Equation

2.3.1 Prescribed surface temperature case

To calculate the energy equation, let us take the new term t as:

$$t = -e^{-\beta\eta} \tag{29}$$

The Eq. (13) calculated as:

$$t\frac{\partial^2\theta}{\partial t^2} + (1 - A_6S_1 - A_6t)\frac{\partial\theta}{\partial t} + A_6\left(2 - \frac{Ni_1}{t}\right)\theta = -A_6Ec_3t \tag{30}$$

where,

$$A_6 = -\frac{(A_4 + Nr)\,\xi_2}{A_5\beta}, Ni_1 = \frac{Ni}{A_5\xi_2\beta}, S_1 = 1 - \frac{S}{D_2}, Ec_3 = -\frac{D_2\beta}{A_5}\left(A_1\beta^2 + A_3M\,\mathrm{Sin}^2(\tau)\right)Ec_1 \tag{31}$$

Modified B. Cs are:

$$\theta(t = -1) = 1, \theta(t = 0) = 0 \tag{32}$$

By utilizing Eqs. (32) and (30) calculated as:

$$\theta(t) = (1 - B_3)(-t)^{B_2}\frac{Laguerre\left[2 - B_2, B_1, A_6t\right]}{Laguerre\left[2 - B_2, B_1, -A_6\right]} + B_3t^2 \tag{33}$$

where, B_1, B_2, and B_3 are defined as:

$$B_1 = \sqrt{A_6^2S_1^2 + 4A_6Ni_1}, B_2 = \frac{A_6S_1 + B_1}{2}, B_3 = \frac{A_6Ec_3}{A_6\left(Ni_1 + 2S_1\right) - 4} \tag{34}$$

Now, the wall temperature gradient calculated as:

$$\theta'(0) = \beta\left(B_3(B_2 - 2) - B_2 + \frac{A_6(1 - B_3)}{(B_1 + 1)}\frac{Laguerre\left[1 - B_2, B_1 + 1, -A_6\right]}{Laguerre\left[2 - B_2, B_1, -A_6\right]}\right) \tag{35}$$

2.3.2 Prescribed heat flux case

By Eqs. (32) and (35), then the PHF Eq. (14) has the same form as Eq. (33) and the parameters in Eq. (34) expect Ec_3 , which is to be replaced here by Ec_4 calculated as:

$$Ec_4 = -\frac{\xi_2 \xi_3}{A_5}\left(A_1 {\xi_3}^2 + A_3 M \sin^2(\tau)\right) Ec_2 \tag{36}$$

Modified B. Cs for PHF case written as:

$$\varphi'(-1) = \frac{1}{D_3}, \varphi(0) = 0 \tag{37}$$

Hence, the solution of the Eq. (14) is given by:

$$\varphi(t) = \frac{\left(2B_3 - {\xi_3}^{-1}\right)(t)^{B_2} Laguerre\left[2 - B_2, B_1, A_6 t\right]}{B_2 L\left[2 - B_2, B_1, -A_6\right] + A_6 (B_1 + 1)^{-1} Laguerre\left[1 - B_2, 1 + B_1, -A_6\right]} + B_3 t^2 \tag{38}$$

Further, the wall temperature is obtained as:

$$\varphi(0) = \frac{\left(2B_3 - {\xi_3}^{-1}\right)(t)^{B_2} Laguerre\left[2 - B_2, B_1, A_6\right]}{B_2 Laguerre\left[2 - B_2, B_1, -A_6\right] + A_6 (B_1 + 1)^{-1} Laguerre\left[1 - B_2, 1 + B_1, -A_6\right]} + B_3 \tag{39}$$

• Dynamic viscosity:

$$\mu_{tnf} = \frac{\mu_f}{(1 - \phi_{SiO_2})^{2.5} (1 - \phi_{Al_2O_3})^{2.5} (1 - \phi_{TiO_2})^{2.5}} \tag{40}$$

• Density:

$$\frac{\rho_{tnf}}{\rho_f} = (1 - \phi_{SiO_2})\left\{(1 - \phi_{Al_2O_3})\left[(1 - \phi_{TiO_2}) + \phi_{TiO_2}\frac{\rho_{TiO_2}}{\rho_f}\right] + \phi_{Al_2O_3}\frac{\rho_{Al_2O_3}}{\rho_f}\right\} + \phi_{SiO_2}\frac{\rho_{SiO_2}}{\rho_f} \tag{41}$$

• Thermal capacitance:

$$\begin{aligned}\frac{(\rho C_p)_{tnf}}{(\rho C_p)_f} &= (1 - \phi_{SiO_2}) \\ &\left\{(1 - \phi_{Al_2O_3})\left[(1 - \phi_{TiO_2}) + \phi_{TiO_2}\frac{(\rho C_p)_{TiO_2}}{(\rho C_p)_f}\right] + \phi_{Al_2O_3}\frac{(\rho C_p)_{Al_2O_3}}{(\rho C_p)_f}\right\} + \phi_{SiO_2}\frac{(\rho C_p)_{SiO_2}}{(\rho C_p)_f}\end{aligned} \tag{42}$$

• Thermal conductivity:

$$\begin{gathered}\frac{\kappa_{tnf}}{\kappa_{hnf}} = \frac{\kappa_{\mathrm{SiO_2}} + 2\kappa_{hnf} - 2\phi_{\mathrm{SiO_2}}(\kappa_{hnf} - \kappa_{\mathrm{SiO_2}})}{\kappa_{\mathrm{SiO_2}} + 2\kappa_{hnf} + \phi_{\mathrm{SiO_2}}(\kappa_{hnf} - \kappa_{\mathrm{SiO_2}})}, \frac{\kappa_{hnf}}{\kappa_{nf}} = \frac{\kappa_{Al_2O_3} + 2\kappa_{nf} - 2\phi_{Al_2O_3}(\kappa_{nf} - \kappa_{Al_2O_3})}{\kappa_{Al_2O_3} + 2\kappa_{nf} + \phi_{Al_2O_3}(\kappa_{nf} - \kappa_{Al_2O_3})}, \\ \frac{\kappa_{nf}}{\kappa_f} = \frac{\kappa_{\mathrm{TiO_2}} + 2\kappa_f - 2\phi_{\mathrm{TiO_2}}(\kappa_f - \kappa_{\mathrm{TiO_2}})}{\kappa_{\mathrm{TiO_2}} + 2\kappa_f + \phi_{\mathrm{TiO_2}}(\kappa_f - \kappa_{\mathrm{TiO_2}})}\end{gathered} \tag{43}$$

• Electrical conductivity:

$$\begin{gathered}\frac{\sigma_{tnf}}{\sigma_{hnf}} = 1 + \frac{3\left(\frac{\sigma_{\mathrm{SiO_2}}}{\sigma_{hnf}} - 1\right)\phi_{\mathrm{SiO_2}}}{\left(\frac{\sigma_{\mathrm{SiO_2}}}{\sigma_{hnf}} + 2\right) - \left(\frac{\sigma_{\mathrm{SiO_2}}}{\sigma_{hnf}} - 1\right)\phi_{\mathrm{SiO_2}}}, \frac{\sigma_{hnf}}{\sigma_{nf}} = 1 + \frac{3\left(\frac{\sigma_{\mathrm{Al_2O_3}}}{\sigma_{nf}} - 1\right)\phi_{\mathrm{Al_2O_3}}}{\left(\frac{\sigma_{Al_2O_3}}{\sigma_{nf}} + 2\right) - \left(\frac{\sigma_{Al_2O_3}}{\sigma_{nf}} - 1\right)\phi_{Al_2O_3}}, \\ \frac{\sigma_{nf}}{\sigma_f} = 1 + \frac{3\left(\frac{\sigma_{\mathrm{TiO_2}}}{\sigma_f} - 1\right)\phi_{\mathrm{TiO_2}}}{\left(\frac{\sigma_{\mathrm{TiO_2}}}{\sigma_f} + 2\right) - \left(\frac{\sigma_{\mathrm{TiO_2}}}{\sigma_f} - 1\right)\phi_{\mathrm{TiO_2}}}\end{gathered} \tag{44}$$

2.3.3 Physical realism and applicability of parameter ranges

Table 1 represents the thermophysical properties of base fluid and nanoparticles. The dimensionless parameter ranges in Table 2 have been chosen in such a way that they correspond to MHD nanofluid flows in porous cooling systems and other similar situations in related applications where the literature has reported the values. The moderate magnetic parameter values limit the magnetic Reynolds number, thereby supporting the assumption of a negligible

induced magnetic field. The inverse Darcy number is representative of porous materials such as metal foams and filtration media. The range of the Eckert number corresponds to the conditions of moderate velocity flows where the viscous dissipation effect is significant, but the boundary layer approximation is still valid. Likewise, the radiation parameter characterizes the condition of elevated temperatures at which radiative heat transfer takes place along with conduction and convection.

The volume fraction of nanoparticles is limited to very low concentrations, as is the case in stable ternary nanofluids; thus, a single-phase model and thermal equilibrium assumption can be adopted. As a result, the present model finds its use in the case of laminar boundary layer flows with low magnetic Reynolds numbers, homogeneous porous media, and well-dispersed nanoparticles. If one considers very high particle loading, strong magnetic induction effects, or turbulent regimes, then the use of advanced multiphase or fully coupled models would be necessary.

Table 1. Thermophysical properties

Properties	H_2O [53]	Al_2O_3 [53, 54]	SiO_2 [53]	TiO_2 [54]
ρ	997.1	3970	2270	4250
C_p	4179	765	730	686
κ	0.6013	40	1.4	8.85
σ	0.05	10^{-12}	3.5×10^6	10^{-10}

Table 2. Physical meaning and practical ranges of dimensionless parameters

Parameter	Physical Meaning	Engineering Relevance	Parameter Range
Λ	Viscosity ratio	Polymer extrusion, microchannels	$0 \leq \Lambda \leq 3$
ϕ	Nanoparticles volume fraction	Stable ternary nanofluids	$0 \leq \phi \leq 0.02$
M	Magnetic field parameter	MHD cooling, magnetic pumps	$0 \leq M \leq 3$
Da^{-1}	Inverse Darcy number	Porous heat exchangers, filtration	$0 \leq Da^{-1} \leq 3$
Nr	Thermal radiation parameter	High-temperature systems	$0 \leq Nr \leq 3$
N_i	Heat source/sink parameter	Reactive or electrically heated systems	$-3 \leq N_i \leq 3$
d	Stretching/shrinking parameter	Sheet extrusion, coating	$-3 \leq d \leq 3$
ξ_1	First-order velocity slip	Micro/nano flows	$0 \leq \xi_1 \leq 3$
ξ_2	Second-order velocity slip	Higher-order rarefaction effects	$0 \leq \xi_2 \leq 3$
S	Mass transpiration parameter	Boundary layer control	$0 \leq S \leq 3$
Pr	Prandtl number	Water-based nanofluids	6.21
Ec_1, Ec_2	Eckert numbers	High shear or high-speed flows	$0 \leq Ec_1, Ec_2 \leq 3$

2.4 Validation

Table 3. Comparison of the current study and related works by other authors

Related Works by Other Authors	Fluids	Value of Momentum Solution
[35]	Newtonian	$\beta = 1$
[6]	Newtonian	$\beta = \sqrt{1+M}$
[36]	Newtonian	$f(\eta) = S + \frac{d}{\beta(1+b\beta)}\left(1 - e^{-\beta\eta}\right)$ $(2+\lambda)b\beta^3 + (2+2\lambda-2bS)\beta^2 - 2S\beta - 2a = 0$
[2]	Newtonian	$f(\eta) = S - \frac{1-e^{\beta\eta}}{\beta}$, $S\beta + (-1+k(m-1))\beta^2 - 1 = 0$
[47]	Newtonian	$f(\eta) = S + \frac{a}{(\beta+b\beta^2)}\left(1 - e^{-\beta\eta}\right)$, $(2+\varepsilon M)b\beta^3 - (2+\varepsilon M - 2SbM)\beta^2 - 2SM\lambda - 2aM = 0$
Present work	Newtonian	$f(\eta) = D_1 + D_2 e^{-\beta\eta}, D_1 = S - D_2, D_2 = \frac{d}{\xi_2\beta^3 - \xi_1\beta^2 - \beta}$ $\Lambda\beta^2 - A_2 S\beta - A_3 M\,\mathrm{Sin}^2(\tau) - A_1 Da^{-1} = 0$

Table 3 demonstrates that the present analytical formulation reduces exactly to several well-established models available in the literature under appropriate limiting assumptions. The comparison confirms that the obtained momentum expressions and characteristic equations are consistent with previously reported results.

2.5 Limiting Cases for Current Analysis with the Earlier Literature

• Excluding volume fraction, radiation, porous media and magnetic field term, viscous dissipation Present results $\rightarrow$ results of Crane [35].

• Excluding permeable medium, ternary nanoparticles,heat dissipation, and including of nano fuid Present results $\rightarrow$ results of Hamid et al. [36].

3 Results and Discussion

The current analysis examines the influence of viscous dissipation, Joule heating, and coupled heat transfer impact on ternary nanofluid flow, a ternary nanofluid formed by dissolving Al_2O_3, SiO_2, and TiO_2 nanoparticles in water. The analysis delves into the formulation of complex PDEs into a more manageable set of ODEs via application of similarity terms. Further examined the energy equation by using Kummer's and Laguerre polynomial methods by incorporating a novel variable; the analysis encompasses both PST and PHF cases, and many physical parameters are studied through graphs; Table 2 defines the physical meaning and practical ranges of parameters.

Figure 2 represents the axial momentum graph for the Da^{-1}, upsurging the Da^{-1} reduces the movement of the fluid. The inverse Darcy number represents the extent to which the porous medium hampers the fluid flow; thus, higher values correspond to lower permeability and more intense drag effects. Increasing this parameter obstructs the flow through the porous medium, thus lowering the velocity and increasing the thickness of the momentum boundary layer. The physical significance is in the interaction of the liquid with the solid matrix of the porous medium, which may result in various flow patterns ranging from laminar to turbulent. Knowledge of such interactions is vital for the accurate prediction and efficient operation of systems that use filtration, oil recovery, and groundwater movement. In porous media situations where better heat transfer performance is required, the ternary nanofluid outperforms the hybrid nanofluid due to its improved thermal transport capacity. However, this improvement causes a slight increase in flow resistance due to the increased effective viscosity generated by the presence of more nanoparticles.

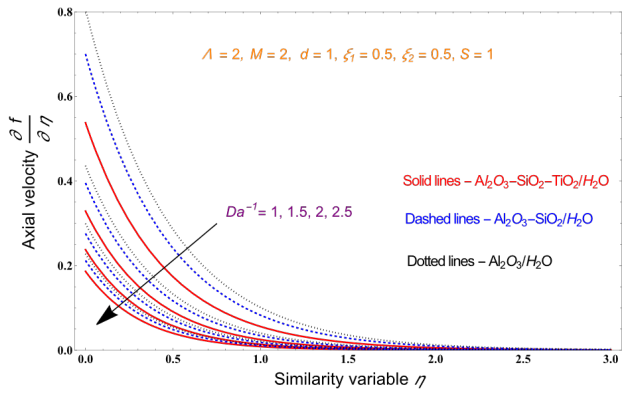


Figure 2. Da^{-1} influence on axial velocity

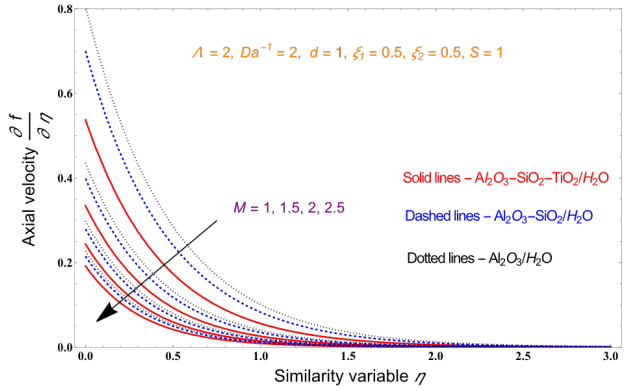


Figure 3. Axial momentum plot for magnetic field

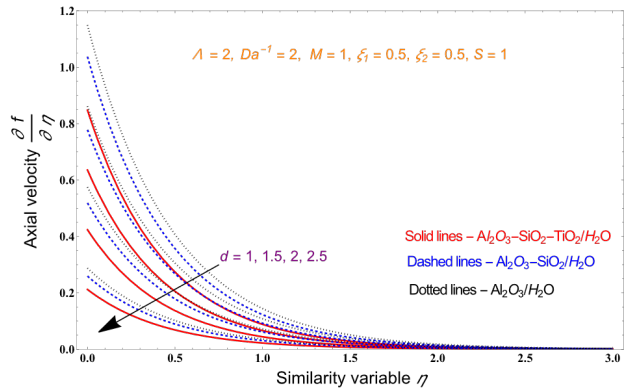
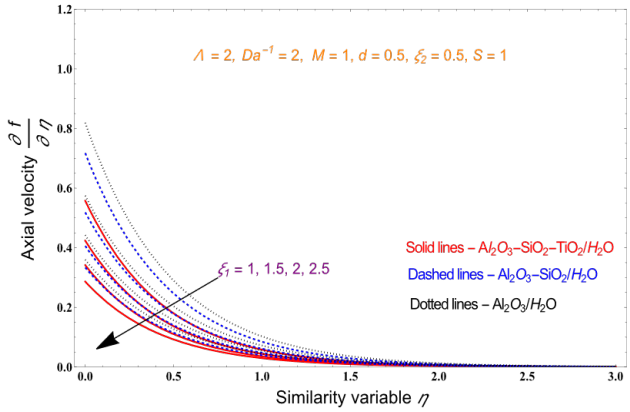
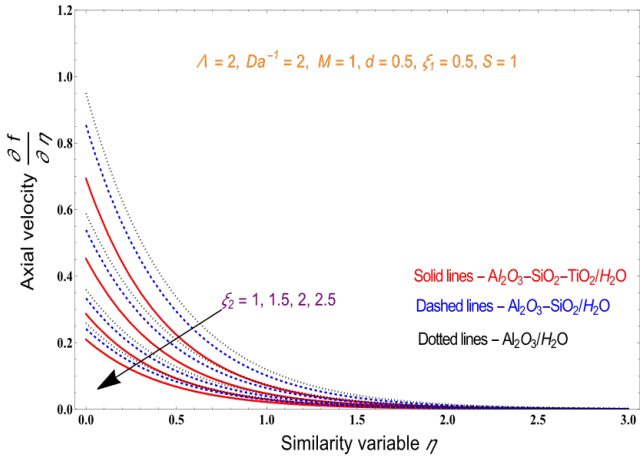


Figure 4. Axial velocity plot for stretching/shrinking term



(a)



(b)

Figure 5. (a) Velocity slip influence on axial velocity; (b) second order slip impact on axial velocity graph

Figure 3 represents the axial velocity graph for the MHD; enhancing the magnetic term reduces the velocity of the fluid movement. When a M term is applied to an electrically conducting fluid, it provides a Lorentz force that opposes the movement of the fluid, effectively altering its momentum. When a magnetic field is applied, a Lorentz force is produced, which acts against the movement of the electrically conducting fluid. Hence, by increasing the magnetic parameter, the fluid velocity is lowered and the momentum boundary layer thickness is also reduced. This interaction can be utilized to control and manipulate the flow in various applications, such as in cooling systems or magnetic pumps. Because of its higher effective thermal conductivity, the ternary nanofluid is more appropriate than the hybrid nanofluid under strong magnetic field situations that call for improved heat transfer. Because of the increased effective viscosity caused by the extra nanoparticles, this benefit results in a minor increase in flow

resistance.

Figure 4 represents the axial velocity graph for the expanding/shrinking term; here solid dashed, and dotted lines denote ternary, hybrid, and nanofluid flow. Upsurging the stretching/shrinking term reduces the momentum; the stretching parameter qualitatively describes the extent to which the surface is stretched or shrunk; hence, it controls the growth of the boundary layer. Increasing the stretching parameter results in a higher surface-induced strain; this changes the velocity profile and causes a change in the thickness of the momentum boundary layer. The stretching/shrinking term significantly influences the momentum, particularly in boundary layer phenomena. When a surface stretches, it tends to accelerate the fluid particles near the surface, enhancing momentum due to the reduction of viscous effects. The ternary nanofluid is preferred to the hybrid nanofluid under higher stretching circumstances that need improved heat transfer due to its increased effective thermal conductivity.

Figure 5a and Figure 5b portray the axial momentum graph for the velocity slips; here solid, dashed, and dotted lines denote ternary, hybrid, and nanofluid movement respectively. upsurging the velocity slips term reduces the momentum of the fluid. The velocity slip is a description of a situation where the fluid at the surface is not fully sticking to the surface but can move slightly in the direction parallel to the wall; thus, a finite tangential velocity is allowed at the boundary. When the slip parameter is increased, the wall shear stress is diminished, resulting in less momentum being extracted from the surface and transferred to the fluid. Hence, the velocity boundary layer reduces in thickness. This parameter accounts for the relative motion between the liquid and the boundary, which can alter the flow's momentum. The ternary nanofluid outperforms the hybrid nanofluid under higher velocity slip situations due to its superior heat transfer capabilities. However, because of the increased effective viscosity brought on by the extra nanoparticles, this advantage causes a slight rise in resistance to flow.

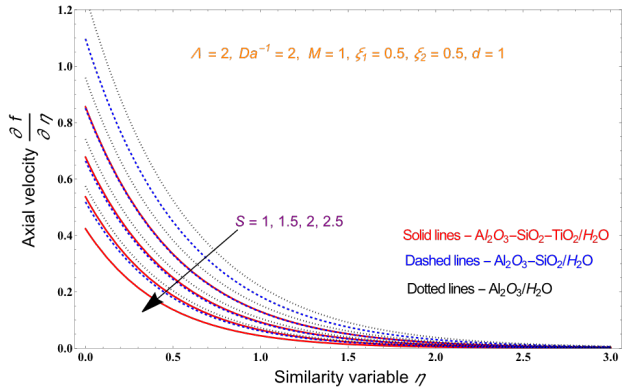


Figure 6. Axial velocity graph for mass transpiration

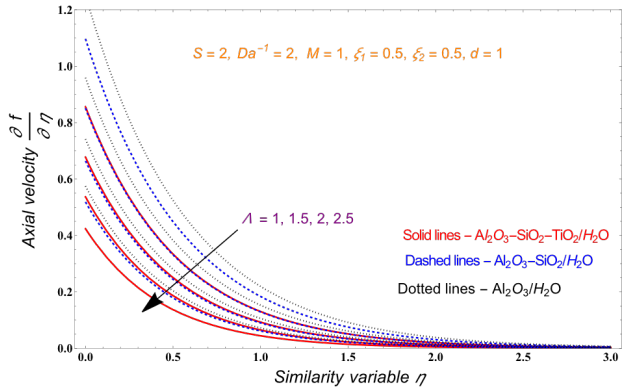


Figure 7. Axial velocity graph for viscosity ratio

Figure 6 portrays the axial velocity plot for the mass transpiration; here solid, dashed and dotted lines portray the ternary, hybrid, and nanofluid movement. Upsurging the mass transpiration reduces the velocity. The suction parameter of mass refers to the removal of fluid from the permeable surface, which leads to the stabilization of the boundary layer. When suction is raised, it makes the velocity boundary layer thinner, and at the same time it halts the motion of fluid near the surface due to the increased mass extraction. The mass transpiration term is crucial in controlling the boundary layer characteristics and ensuring the stability of the flow. Under the higher suction conditions, the ternary nanofluid performs better than the hybrid nanofluid because of its enhanced thermal transport

properties. This gain comes with a modest increase in flow resistance since the added nanoparticles increase the fluid's effective viscosity.

Figure 7 portrays the axial velocity plot for the viscosity ratio; here, solid, dashed, and dotted lines denote ternary, hybrid, and nanofluid flow. Upsurging the viscosity ratio term reduces the momentum of the fluid flow. The viscosity ratio reveals the share of the effective nanofluid viscosity in total viscosity and, hence, the change in flow resistance due to nanoparticle dispersion. It is well understood that a higher viscosity ratio increases the internal fluid friction that in turn lowers the velocity profile and makes the momentum diffusion effects more powerful. Physically, the ratio of viscous heat production to heat conduction in a moving viscous fluid is measured by the dimensionless viscosity ratio. It is frequently applied in polymer processing to measure the impact of heat transfer caused by viscous dissipation. Because of its superior thermal characteristics, the ternary nanofluid becomes more favorable than the hybrid nanofluid when higher thermal transfer performance is needed. However, the introduction of extra nanoparticles increases the fluid's effective viscosity, resulting in a modest increase in flow resistance.

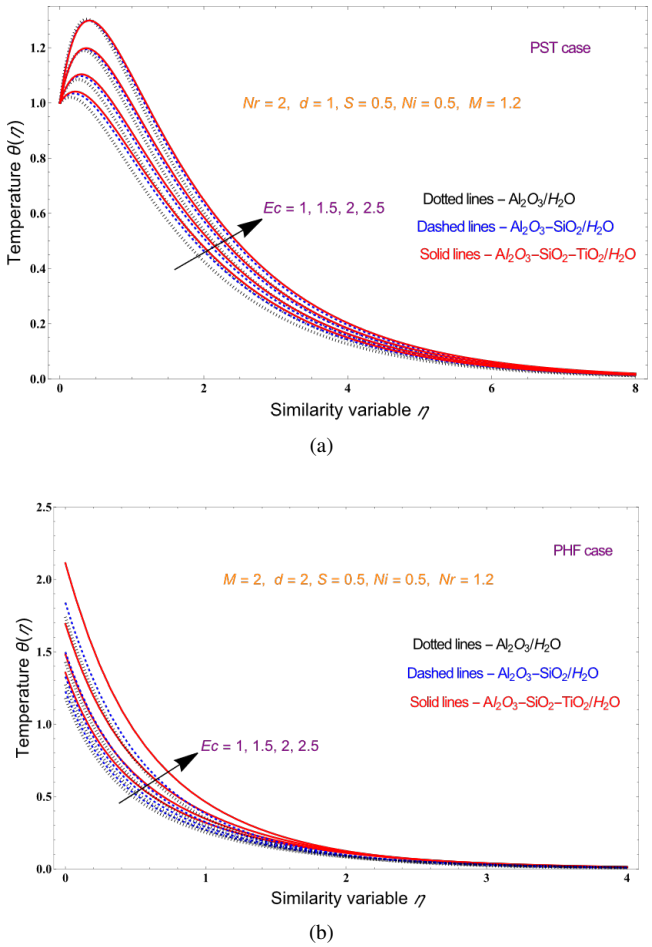
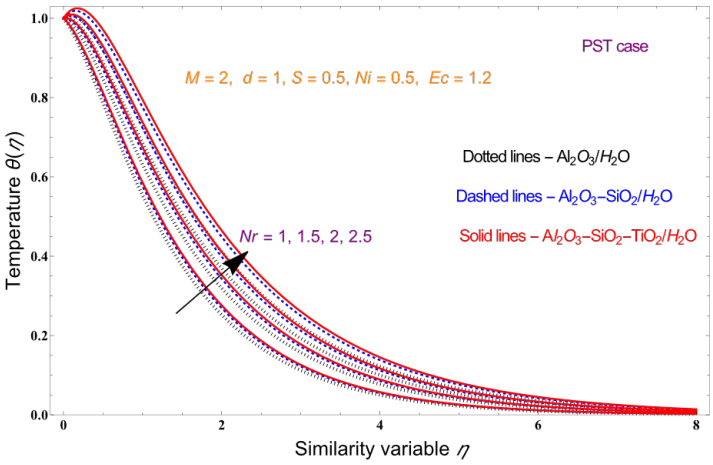
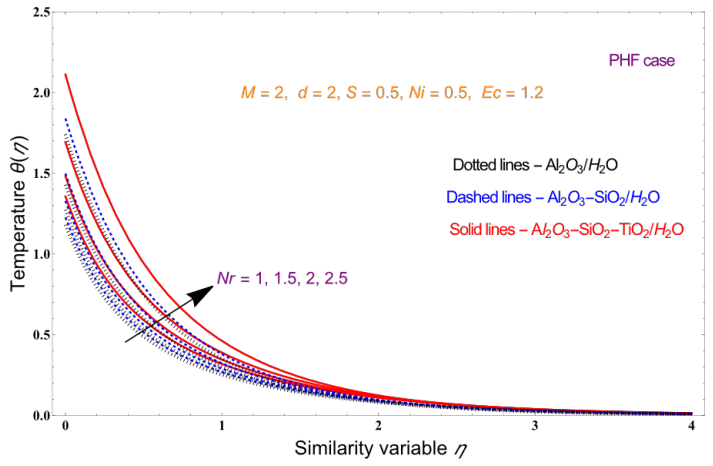


Figure 8. (a) Eckert number influence on prescribed surface temperature (PST) temperature; (b) Eckert number influence on prescribed heat flux (PHF) temperature

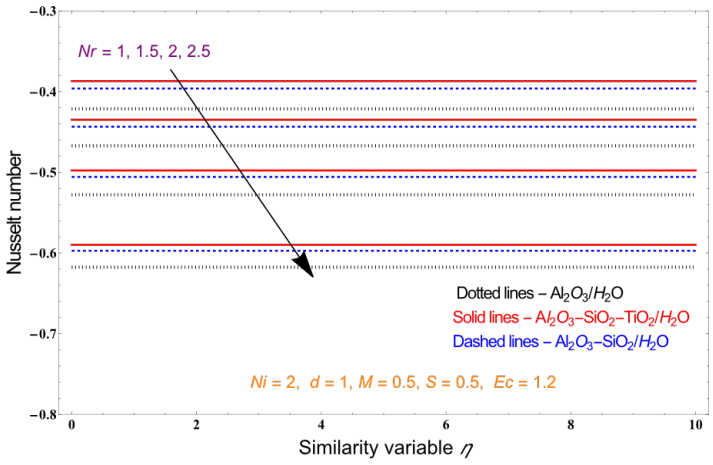
Figure 8a and Figure 8b represent the temperature plots for the Eckert term for both PST and PHF cases; here solid, dashed, and dotted lines portray ternary, hybrid, and nanofluid movement respectively. Eckert number quantifies the portion of kinetic energy that is transformed into internal energy by viscous dissipation. Under either PST or PHF, the fluid temperature is raised and the thermal boundary layer is thickened as the Eckert number increases because of the stronger internal heat generation; upsurging the Eckert number term raises the energy of the liquid movement. Physically, it denotes the ratio of the flow's kinetic energy to its enthalpy change, providing insight into the influence of fluid velocity on energy distribution. A high Eckert number denotes that the kinetic energy is significant compared to thermal energy, which can lead to notable temperature increases due to viscous dissipation. At higher Eckert number conditions, the ternary nanofluid exhibits superior thermal behavior compared with the hybrid nanofluid because it more effectively converts viscous dissipation into internal energy. Because of the increased effective viscosity brought on by the extra nanoparticles, this enhanced heat transfer is accompanied by a little increase in flow resistance.



(a)



(b)



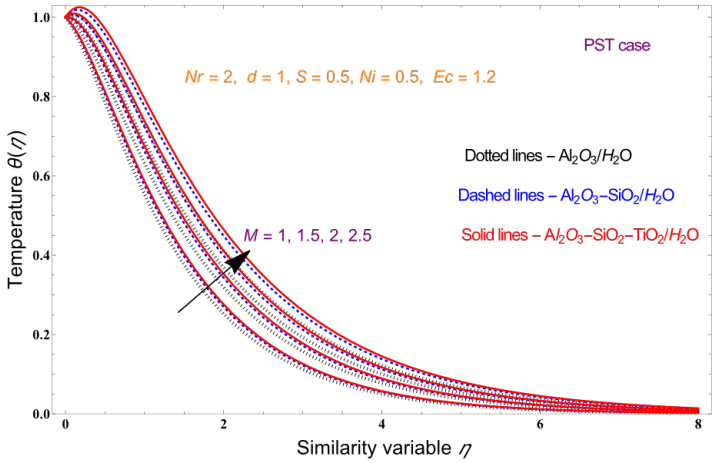
(c)

Figure 9. (a) Temperature plot for thermal radiation prescribed surface temperature (PST) case; (b) thermal radiation impact on temperature prescribed heat flux (PHF) case; (c) Nusselt number graph for thermal radiation

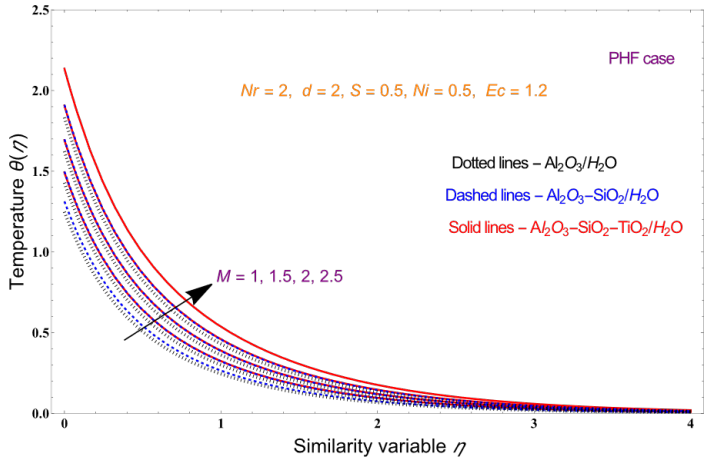
Figure 9a and Figure 9b depict the temperature graphs for the Nr for both PST and PHF cases; here solid, dashed, and dotted lines denote ternary, hybrid, and nanofluid flow respectively. Raising the thermal radiation raises the energy of the liquid movement. Figure 9c denotes the Nusselt number graph for thermal radiation. An increase the thermal radiation reduces the Nusselt number; a rise in the thermal radiation term typically results in a higher

fluid temperature.

The thermal radiation parameter characterizes the impact of radiative heat transfer in comparison to conductive heat transfer within the fluid. When this parameter increases, energy transport by radiation is enhanced, which consequently leads to an increase in fluid temperature and a thicker thermal boundary layer. This is due to the enhanced energy absorption by the fluid, which can be particularly pronounced when there is a large energy difference between the liquid and its surroundings. Under strong thermal radiation conditions, the ternary nanofluid performs better than the hybrid nanofluid because of its higher effective thermal conductivity and improved heat transfer capability. Because of the increased effective viscosity brought on by the extra nanoparticles, this improvement is accompanied by a little increase in flow resistance.



(a)



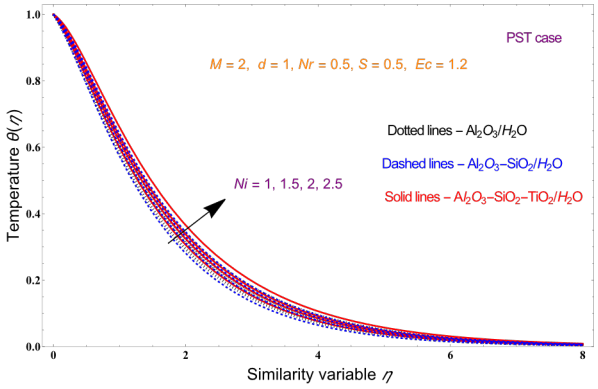
(b)

Figure 10. (a) Temperature plot for magnetic field prescribed surface temperature (PST) case; (b) temperature plot for magnetic field prescribed heat flux (PHF) case

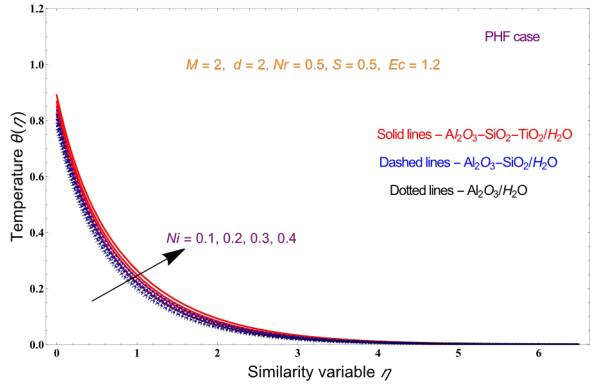
Figure 10a and Figure 10b portray the energy plots for MHD on both PST and PHF cases; here solid, dashed, and dotted lines depict ternary, hybrid, and nanofluid, respectively. Raising the magnetic field raises the temperature of the fluid flow. In both heat boundary conditions, i.e., with PST and PHF, the magnetic field induces a resistive Lorentz force that converts the velocity energy into thermal energy via Joule heating. Hence, increasing the magnetic parameter leads to an increase in the temperature of the fluid and, consequently, to the enhancement of the thermal boundary layer thickness in both thermal boundary cases; magnetic fields can raise heat transfer in microscale flows between parallel plates, affecting the energy distribution. Furthermore, because of the combined thermal conductivity of many nanoparticles, the ternary nanofluid exhibits higher temperature enhancement under strong magnetic field circumstances than hybrid and mono nanofluids. However, because the ternary nanofluid's effective viscosity is comparatively greater than the hybrid nanofluid's, this enhanced thermal performance is accompanied by a little increase in flow resistance.

Figure 11a and Figure 11b portray the energy plots for the heat source/sink for both PST and PHF cases, enhancing

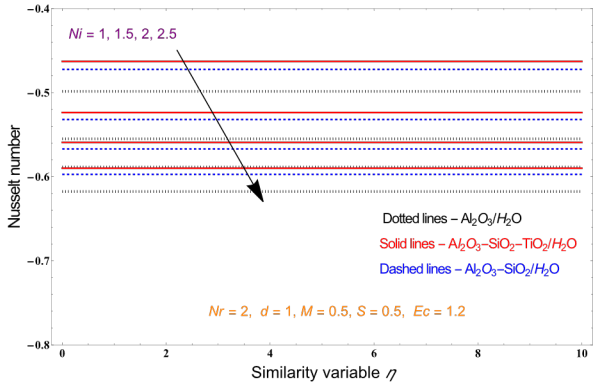
the heat source/sink upsurge of the energy of the fluid. Figure 11c denotes the Nusselt number plot for the heat source/sink. As the heat source/sink increases, the Nusselt term decreases, which denotes the ratio of convective to conductive heat exchanging at the boundary of a fluid movement. In both PST and PHF scenarios, the presence of a positive heat source parameter results in additional heat inside the system; thus, the temperature of the fluid is raised. When the rate of heat generation increases, the temperature layer near the surface becomes more extended, whereas a heat sink results in the local cooling effect. An upsurge in the heat source intensity typically raises the fluid temperature and enhances the convective heat transfer, tending toward an upper Nusselt term. This signifies a more efficient heat transfer from the surface to the liquid, which is essential in designing effective cooling systems and understanding the thermal behavior of fluids. Because of its enhanced thermal conductivity and heat transfer ability, the ternary nanofluid is more appropriate than the hybrid nanofluid in situations of intense heat production and high thermal gradients. Nevertheless, this enhancement slightly increases the flow resistance because more nanoparticles increase the fluid's effective viscosity.



(a)



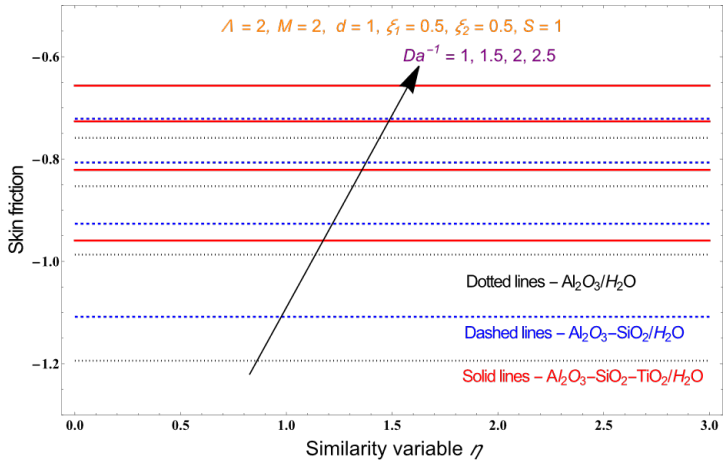
(b)



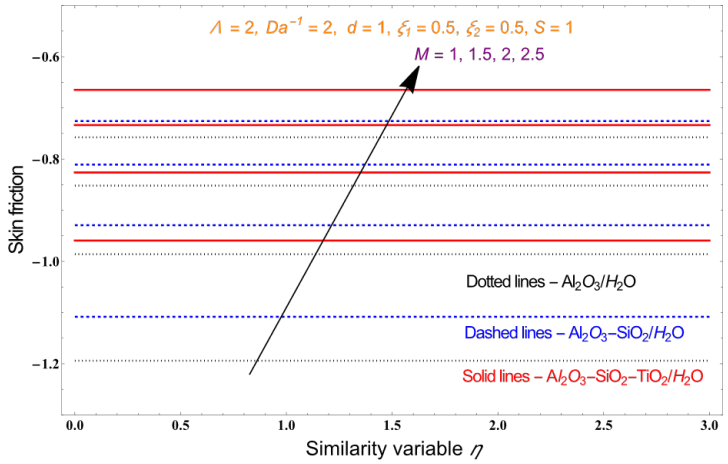
(c)

Figure 11. (a) Temperature plot for heat source/sink prescribed surface temperature (PST) case; (b) heat source impact on prescribed heat flux (PHF) temperature; (c) Nusselt number graph for heat source/sink

Figure 12a and Figure 12b portray the skin friction graphs for the Da^{-1} and MHD; here solid, dashed, and dotted lines represent ternary, hybrid, and nanofluids, upsurging the magnetic field and Da^{-1} decreasing the skin friction of the fluid flow. Enhancing the magnetic field causes the Lorentz force to become stronger, which is a force that acts to resist the fluid motion and, as a result, changes the wall shear stress, thus causing an increase in skin friction. On the other hand, a bigger inverse Darcy number makes porous medium resistance more dominant, hence the momentum getting suppressed near the surface and the skin friction coefficient becoming larger. From a practical perspective, the ternary nanofluid provides better thermal performance than the hybrid nanofluid, although it leads to a modest rise in skin friction. Therefore, despite the minor increase in flow resistance, the ternary nanofluid is more appropriate for situations where improved heat transfer is preferred.



(a)



(b)

Figure 12. (a) Skin friction graph for Da^{-1}; (b) skin friction plot for the magnetic field

Figure 13 portrays the streamlined plots for various choices of viscosity ratio, MHD, and inverse Darcy term; here solid, dashed, and dotted lines denote ternary, hybrid, and nanofluid movement, respectively. Increasing the magnetic parameter will strengthen the Lorentz force, which, by enhancing the resistance to fluid motion, will change the wall shear stress and thus increase skin friction. Similarly, a larger inverse Darcy number will increase the level of resistance of the porous medium, which will elevate momentum suppression near the surface and thus increase the skin friction coefficient. The streamline snapshots illustrate that an increase in the viscosity ratio causes a significant reduction in the fluid circulation because of stronger internal friction, thus resulting in more compact and quite weakly flowing structures near the surface. The Lorentz force, which is the result of an increase in the magnetic parameter, acts against the primary flow direction; thus, the strength of the vortical motion is decreased, and the streamlines are pushed to the boundary. A higher inverse Darcy number similarly means that the porous medium offers a higher degree of resistance; this results in the suppression of fluid penetration and the diminishing of recirculation zones. A larger viscosity ratio, a stronger magnetic field, and an increased porous resistance are the factors that together exert such influence that the flow configuration gets a major damping, features of which include

a reduced streamline spacing as well as lower momentum transport in general.

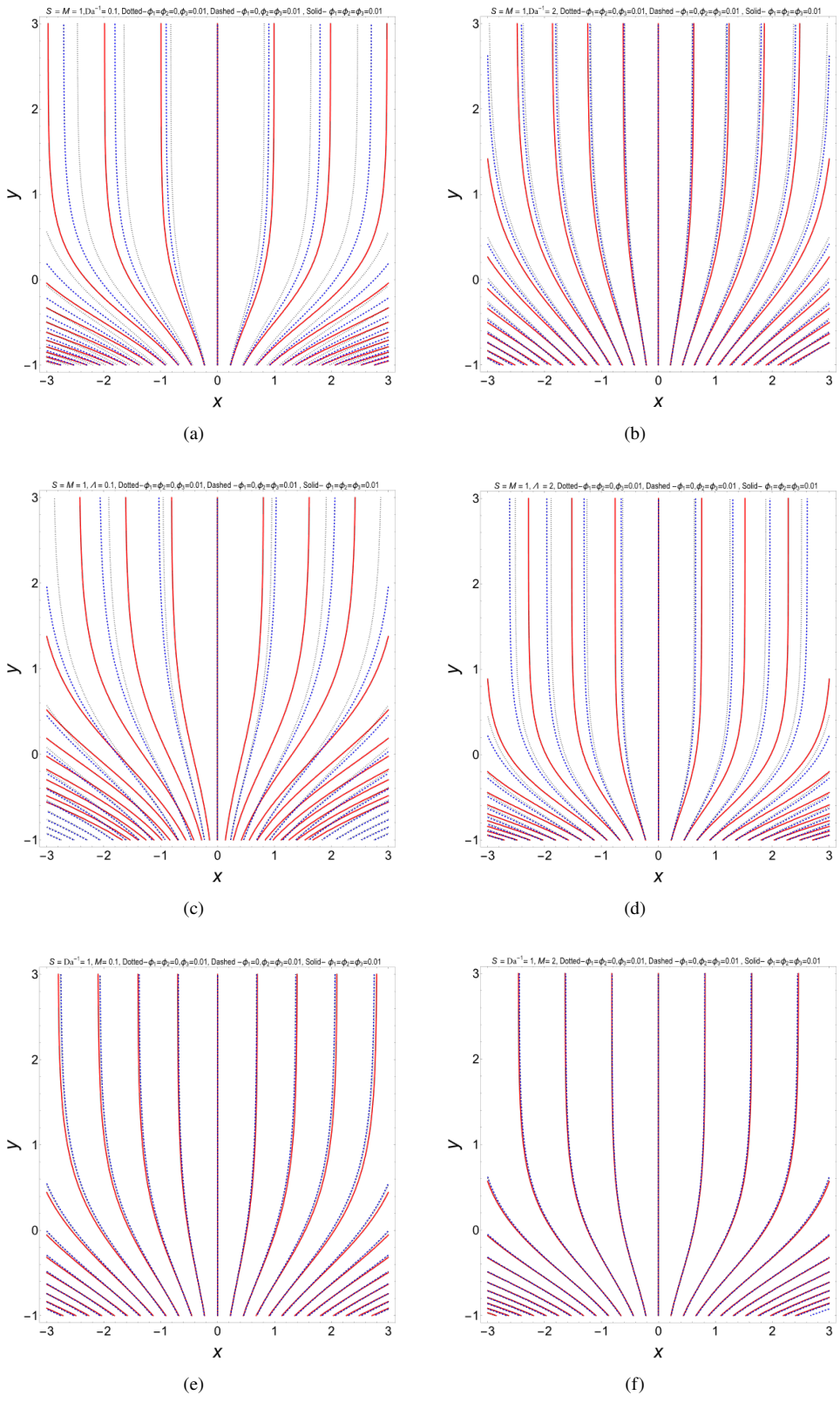


Figure 13. (a) Streamline graph for inverse Darcy number value 0.1; (b) streamline graph for inverse Darcy number value 2; (c) streamline graph for viscosity ratio value 0.1; (d) streamline graph for viscosity ratio term value 2; (e) streamline graph for magnetic field value 0.1; (f) streamline graph for magnetic field value 2

3.1 Practical Significance of Ternary Nanofluid Formulation

The comparative profiles of hybrid nanofluid (Al_2O_3-SiO_2/H_2O) and ternary nanofluid (Al_2O_3-SiO_2-TiO_2/H_2O) show that the ternary suspension gives a higher thermal performance due to the synergistic effect of the three different types of nanoparticles. As seen also in Figure 9b and Figure 9c, the ternary nanofluid shows higher temperature levels and a different behavior of Nusselt number with the usage of thermal radiation; in other words, it is capable of stronger energy absorption and heat transport than the hybrid one.

Nevertheless, this thermal improvement goes hand-in-hand with the increased difficulty of the flow. Figure 12a and Figure 12b illustrate that the ternary nanofluid gives larger skin friction coefficients than the hybrid nanofluid at the same inverse Darcy number; the reason for this is the higher effective viscosity of the ternary mixture. As a consequence, a more powerful pump will be needed to maintain the flow. So, the findings disclose the existence of a trade-off in practice: on the one hand, ternary nanofluids possess outstanding heat transfer abilities; on the other hand, they cause a rise in hydrodynamic drag. Such fluids find their greatest use in a situation where the biggest heat rejection is the primary concern rather than the smallest flow resistance, e.g., in the cooling of very powerful electronics and in compact thermal systems.

4 Comparative Analysis of Prescribed Surface Temperature and Prescribed Heat Flux Boundary Conditions

Although both PST and PHF conditions depict the thermal transport at the wall, they portray fundamentally different thermal control mechanisms. In the PST case, the wall temperature is fixed, and the thermal boundary layer adjusts by altering the temperature gradient at the sheet. In contrast, under PHF cases, the wall heat flux is specified, and the sheet temperature becomes part of the solution.

This distinction leads to various thermal sensitivities. In the PST case, variations in parameters such as the Eckert number, radiation term, and heat source primarily impact the wall temperature gradient and thus the Nusselt number. However, in the PHF configuration, these terms influence both the wall temperature and the thermal gradient, producing a different quantitative energy transfer response. Therefore, the choice of boundary condition plays an important role in determining thermal boundary layer characteristics in magnetized ternary nanofluid flow.

4.1 Quantitative Comparison of Prescribed Surface Temperature and Prescribed Heat Flux Responses

A quantitative analysis of the temperature profiles reveals that the PHF arrangement changes its temperature more drastically with changes in the thermal parameters than the PST case. Thus, the radiation parameter change increases the temperature by only about 12% under PST, while the same parameter change increases the temperature under PHF by almost 18%. The same kind of trend is evidenced by the Eckert number, where viscous dissipation increases temperature by around 15% for PST but about 22% for PHF conditions.

The main reason for this difference is that, in the PST case, the wall temperature is kept constant, so the potential for thermal variation is limited, whereas in the PHF configuration, the wall temperature is allowed to change in accordance with the heat flux, thereby amplifying the overall thermal response. Thus, PHF boundary conditions result in thermal components being more sensitive to slight changes, while PST conditions offer temperature regulation with less fluctuation.

Table 4 shows a quantitative comparison of the percentage variations in the temperature distribution for both PST and PHF conditions, as well as the changes in the skin friction coefficient and Nusselt number for specific governing parameters. The magnetic parameter M improves thermal responsiveness by 20% in the PST case and 25% in the PHF case, while also increasing skin friction coefficient by roughly 30% owing to resistive Lorentz force. The Eckert number Ec which represents viscous dissipation, leads to a considerable increase in temperature in both thermal boundary conditions. Furthermore, the inverse Darcy number raises the skin friction coefficient by around 32%, suggesting higher resistance provided by the porous medium. The thermal radiation parameter Nr and heat source/sink parameter Ni have significant influence on the temperature field and Nusselt number, illustrating the sensitivity of heat transfer characteristics to these factors.

Table 4. Quantitative comparison of the percentage changes in temperature profiles for prescribed surface temperature (PST) and prescribed heat flux (PHF) cases

Parameter	Temperature (%)		Skin Friction (%)	Nusselt Number (%)
	PST	PHF		
M (Magnetic parameter)	20%	25%	30%	-
Ec (Eckert number)	15%	22%	-	-
Da^{-1} (Inverse Darcy number)	-	-	32%	-
Nr (Thermal radiation)	12%	18%	-	9%
N_i (Heat source/sink)	27%	24%	-	26%

4.2 Computational Implementation and Parametric Evaluation

Although closed-form analytical expressions were gained for the momentum and temperature fields, the evaluation of these solutions across a wide parameter range requires systematic computational implementation. The roots of the momentum equation were first computed for each term set to ensure physically admissible reducing solutions. The analytical solutions involving exponential functions and generalized Laguerre polynomials were then evaluated analytically.

Parameter sweeps were performed by changing one parameter at a time while keeping others fixed within physically realistic ranges, as summarized in Section 4.1. For each term combination, the momentum profile, energy distribution, reduced skin friction coefficient, and Nusselt number were calculated. Graphical outcomes were produced by discretizing the similarity variable across a sufficiently large domain to ensure asymptotic convergence of the boundary layer.

Standard analytical methods were used for the root's evaluation and special functions implementation in all calculations. It was ensured that the temperature solution converges for various values of the radiation and dissipation terms. This efficient computational protocol makes the analytical platform accessible for scientific-type parametric analysis.

5 Conclusion

The present study examined the behavior of dissipative ternary nanofluid flow over a permeable surface in the presence of viscous dissipation, Joule heating, and coupled heat-transfer effects. The ternary nanofluid, composed of Al_2O_3, SiO_2, and TiO_2 nanoparticles dispersed in water, was analysed under both PST and PHF conditions. By means of suitable similarity transformations, the governing equations were reduced to a tractable form, which made it possible to assess the influence of the main physical parameters on the velocity and thermal fields. The principal findings may be summarised as follows:

• An increase in the magnetic parameter suppresses the fluid velocity while increasing the skin-friction coefficient and the thermal field in both PST and PHF cases.

• A stronger porous-medium resistance reduces the momentum boundary layer and increases wall shear.

• Higher mass transpiration and stronger stretching/shrinking effects reduce the fluid momentum.

• An increase in the viscosity-ratio parameter weakens the velocity boundary layer.

• Larger values of the Eckert number enhance the temperature field under both PST and PHF boundary conditions.

• Thermal radiation increases the temperature distribution and reduces the Nusselt number.

• A stronger heat source parameter raises the fluid temperature.

Overall, the results confirm that viscous dissipation and Joule heating have a pronounced influence on the thermal response of the system, whereas magnetic and porous-medium effects play an important role in controlling the flow structure. The combined action of these parameters determines the balance between heat-transfer enhancement and flow resistance in ternary nanofluid transport over permeable surfaces.

5.1 Engineering Implications of the Present Study

The present results may be useful in the design of magnetically controlled thermal systems involving ternary nanofluids in porous structures. In particular, the analysis shows that parameters such as viscous dissipation and thermal radiation can significantly increase the fluid temperature, which may be beneficial in processes where enhanced thermal transport is required. At the same time, stronger magnetic effects and greater porous resistance provide additional means of flow control, although these advantages are accompanied by reduced velocity and increased wall shear, which may lead to a higher pumping-power requirement. The ternary nanofluid considered here is expected to offer better thermal performance than conventional or hybrid nanofluids, but this improvement is not without cost. The gain in heat-transfer capability is associated with increased hydrodynamic resistance, and this trade-off must be considered in practical design. From an engineering point of view, the best operating condition is therefore not obtained simply by maximising thermal enhancement but by selecting parameter combinations that improve heat removal without causing excessive flow resistance or undesirable thermal buildup near the surface.

For this reason, the present model may serve as a useful predictive framework for the preliminary design and optimisation of advanced cooling technologies, porous heat exchangers, and other thermal-management systems in which coupled magnetic, porous, and dissipative effects are relevant.

5.2 Limitations and Future Work

The present analysis is limited to a steady, laminar, two-dimensional boundary-layer flow model based on a single-phase representation of the ternary nanofluid. The thermophysical properties are assumed to be constant, and the induced magnetic field is neglected. These assumptions make the problem analytically tractable, but they also restrict the direct applicability of the model to more complex operating conditions.

In particular, when the nanoparticle concentration becomes high, when the magnetic field is very strong, or when non-Darcy porous effects become significant, the present formulation may no longer provide an adequate physical description. Under such conditions, a fully coupled numerical treatment beyond the boundary-layer approximation may be required. In addition, the single-phase effective-property approach does not account for particle interaction, agglomeration, slip mechanisms, or local thermal non-equilibrium effects, all of which may become important at higher particle loadings.

Future work may therefore consider unsteady flow, variable thermophysical properties, non-Newtonian base fluids, entropy-generation analysis, and experimental validation. Such extensions would provide a broader basis for assessing the practical relevance of the present model and for improving its applicability to real engineering systems.

5.3 Applicability of the Analytical Solutions

The analytical solutions obtained in this study are valid within the framework of laminar boundary-layer theory and for parameter ranges consistent with the assumptions used in the derivation. They are therefore most appropriate for physically moderate regimes in which the flow remains steady, two-dimensional, and sufficiently close to the boundary-layer structure adopted in the analysis.

If the magnetic field becomes excessively strong, or if viscous dissipation and Joule heating become dominant, the coupled nonlinear effects may become too pronounced for the present analytical framework to remain fully reliable. In such cases, the flow may depart from the assumed boundary-layer behaviour, and a fully numerical approach would be more appropriate. Similarly, the Darcy-Brinkman porous-medium model adopted here assumes homogeneous permeability and cannot represent more complex situations involving anisotropic, heterogeneous, or strongly non-Darcy porous structures.

It should also be noted that the ternary nanofluid has been modeled through an effective-property single-phase approach. At higher particle concentrations, additional physical mechanisms such as inter-particle interaction, agglomeration, slip velocity, and thermal non-equilibrium may become important and would require more advanced multiphase or two-component formulations. Accordingly, the present analytical solutions should be interpreted as valid for the class of physical situations described above and not as universally applicable to all ternary nanofluid systems.

Author Contributions

Conceptualization, K.N. and S.M.S.; methodology, S.M.S. and U.S.M.; validation, U.S.M. and L.M.P.; formal analysis, S.M.S.; investigation, S.M.S.; resources, S.M.S and K.N.; data curation, S.M.S and K.N.; writing—original draft preparation, S.M.S.; writing—review and editing, U.S.M. and G.L.; visualization, K.N.; supervision, U.S.M.; project administration, G.L. and U.S.M. All authors were actively involved in discussing the findings and refining the final manuscript.

Data Availability

The data used to support the findings of this study are available from the corresponding author upon request.

Conflicts of Interest

The authors declare that they have no conflicts of interest.

References

[1] S. Dolui, B. Bhaumik, and S. De, "Combined effect of induced magnetic field and thermal radiation on ternary hybrid nanofluid flow through an inclined catheterized artery with multiple stenosis," *Chem. Phys. Lett.*, vol. 811, p. 140209, 2023. https://doi.org/10.1016/j.cplett.2022.140209

[2] M. Turkyilmazoglu, "Flow of a micropolar fluid due to a porous stretching sheet and heat transfer," *Int. J. Non-Linear Mech.*, vol. 83, pp. 59–64, 2016. https://doi.org/10.1016/j.ijnonlinemec.2016.04.004

[3] S. U. Jan, U. Khan, M. A. El-Rahman, S. Islam, A. M. Hassan, and A. Ullah, "Effect of variable thermal conductivity of ternary hybrid nanofluids over a stretching sheet with convective boundary conditions and magnetic field," *Results Eng.*, vol. 20, p. 101531, 2023. https://doi.org/10.1016/j.rineng.2023.101531

[4] N. K. Mishra, B. K. Sharma, P. Sharma, T. Muhammad, and L. M. Pérez, "Entropy generation optimization of cilia regulated MHD ternary hybrid Jeffery nanofluid with Arrhenius activation energy and induced magnetic field," *Sci. Rep.*, vol. 13, no. 1, p. 14483, 2023. https://doi.org/10.1038/s41598-023-41299-8

[5] H. Chen, Y. Ma, M. Shen, P. He, and H. Zhang, "Significance of Cattaneo-Christov double diffusion and induced magnetic field on Maxwell ternary nanofluid flow with magnetic response boundary," *J. Magn. Magn. Mater.*, vol. 587, p. 171264, 2023. https://doi.org/10.1016/j.jmmm.2023.171264

[6] K. B. Pavlov, "Magnetohydrodynamic flow of incompressible viscous fluid caused by of a surface," *Magn. Gidrodin.*, vol. 4, pp. 146–147, 1974.

[7] L. Zhang, M. M. Bhatti, and E. E. Michaelides, "Electro-magnetohydrodynamic flow and heat transfer of a third-grade fluid using a Darcy-Brinkman-Forchheimer model," *Int. J. Numer. Methods Heat Fluid Flow*, vol. 31, no. 8, pp. 2623–2639, 2020. https://doi.org/10.1108/HFF-09-2020-0566

[8] W. Yao, Z. Shen, and G. Ding, "Simulation of interstitial fluid flow in ligaments: Comparison among stokes, brinkman and darcy models," *Int. J. Biol. Sci.*, vol. 9, no. 10, pp. 1050–1056, 2013. https://doi.org/10.7150/ijbs.7242

[9] K. Murali, V. Kesavulu Naidu, and B. Venkatesh, "Solution of Darcy-Brinkman-Forchheimer equation for irregular flow channel by finite elements approach," *J. Phys. Conf. Ser.*, vol. 1172, p. 012033, 2019. https://doi.org/10.1088/1742-6596/1172/1/012033

[10] C. P. Tso and S. P. Mahulikar, "The role of the Brinkman number in analysing flow transitions in microchannels," *Int. J. Heat Mass Transfer*, vol. 42, no. 10, pp. 1813–1833, 1999. https://doi.org/10.1016/S0017-9310(98)00276-2

[11] Ò. À. Bèg, H. S. Takhar, and V. M. Soundalgekar, "Thermoconvective flow in a saturated, isotropic, homogeneous porous medium using Brinkman's model: Numerical study," *Int. J. Numer. Methods Heat Fluid Flow*, vol. 8, no. 5, pp. 559–589, 1998. https://doi.org/10.1108/09615539810220298

[12] M. K. Nayak, S. Shaw, V. S. Pandey, and A. J. Chamkha, "Combined effects of slip and convective boundary condition on MHD 3D stretched flow of nanofluid through porous media inspired by non-linear thermal radiation," *Indian J. Phys.*, vol. 92, no. 8, pp. 1017–1028, 2018. https://doi.org/10.1007/s12648-018-1188-2

[13] Y. Leng, S. Li, S. Algarni, W. Jamshed, T. Alqahtani, R. W. Ibrahim, K. Irshad, F. A. A. ElSeabee, and A. M. Hassan, "Computational study of magnetized and dual stratified effects on non-Darcy Casson nanofluid flow: An activation energy analysis," *Case Stud. Therm. Eng.*, vol. 53, p. 103804, 2024. https://doi.org/10.1016/j.csite.2023.103804

[14] N. S. Kaingu, N. Joel, M. W. Nduku, J. Okelo, and K. Awuor, "Effects of activation energy on reactive MHD flows with joule heating," *World J. Res. Rev.*, vol. 15, no. 6, pp. 9–17, 2023. https://doi.org/10.31871/WJRR.15.6.5

[15] M. Nazeer, N. Ali, F. Ahmad, W. Ali, A. Saleem, Z. Ali, and A. Sarfraz, "Effects of radiative heat flux and joule heating on electro-osmotically flow of non-Newtonian fluid: Analytical approach," *Int. Commun. Heat Mass Transfer*, vol. 117, p. 104744, 2020. https://doi.org/10.1016/j.icheatmasstransfer.2020.104744

[16] S. A. Khan, M. Imran Khan, S. A. M. Alsallami, S. Alhazmi, F. M. Alharbi, and E. R. El-Zahar, "Irreversibility analysis in hydromagnetic flow of Newtonian fluid with Joule heating: Darcy-Forchheimer model," *J. Pet. Sci. Eng.*, vol. 212, p. 110206, 2022. https://doi.org/10.1016/j.petrol.2022.110206

[17] S. M. Sachhin, F. J. Granados-Ortiz, U. S. Mahabaleshwar, J. Ortega-Casanova, and L. M. Pérez, "Heat and mass transfer analysis of a Bingham ternary nanofluid exposed to radiation over stretching/shrinking sheets and Stefan blowing effect," *Alex. Eng. J.*, vol. 129, pp. 515–529, 2025. https://doi.org/10.1016/j.aej.2025.06.026

[18] P. K. Pattnaik, S. R. Mishra, O. Anwar Bég, U. F. Khan, and J. C. Umavathi, "Axisymmetric radiative titanium dioxide magnetic nanofluid flow on a stretching cylinder with homogeneous/heterogeneous reactions in Darcy-Forchheimer porous media: Intelligent nanocoating simulation," *Mater. Sci. Eng. B*, vol. 277, p. 115589, 2022. https://doi.org/10.1016/j.mseb.2021.115589

[19] O. A. Bég, M. S. Khan, I. Karim, M. M. Alam, and M. Ferdows, "Explicit numerical study of unsteady hydromagnetic mixed convective nanofluid flow from an exponentially stretching sheet in porous media," *Appl. Nanosci.*, vol. 4, no. 8, pp. 943–957, 2013. https://doi.org/10.1007/s13204-013-0275-0

[20] I. Waini, A. Ishak, T. Groşan, and I. Pop, "Mixed convection of a hybrid nanofluid flow along a vertical surface embedded in a porous medium," *Int. Commun. Heat Mass Transfer*, vol. 114, p. 104565, 2020. https://doi.org/10.1016/j.icheatmasstransfer.2020.104565

[21] V. K. Joshi, P. Ram, D. Tripathi, and K. Sharma, "Numerical investigation of magnetic nanofluids flow over rotating disk embedded in a porous medium," *Therm. Sci.*, vol. 22, no. 6 Part B, pp. 2883–2895, 2018. https://doi.org/10.2298/TSCI170323139J

[22] J. Wang, Y.-P. Xu, R. Qahiti, M. Jafaryar, M. A. Alazwari, N. H. Abu-Hamdeh, A. Issakhov, and M. M. Selim, "Simulation of hybrid nanofluid flow within a microchannel heat sink considering porous media analyzing CPU stability," *J. Pet. Sci. Eng.*, vol. 208, p. 109734, 2022. https://doi.org/10.1016/j.petrol.2021.109734

[23] S. M. Sachhin, P. K. Ankitha, G. M. Sachin, U. S. Mahabaleshwar, I. V. Shevchuk, S. N. R. Nayakar, and R. Kadli, "Chemically reactive micropolar hybrid nanofluid flow over a porous surface in the presence of an inclined magnetic field and radiation with entropy generation," *Physics*, vol. 6, no. 4, pp. 1315–1344, 2024. https://doi.org/10.3390/physics6040082

[24] D. Yu and R. Wang, "An optimal investigation of convective fluid flow suspended by carbon nanotubes and thermal radiation impact," *Mathematics*, vol. 10, no. 9, p. 1542, 2022. https://doi.org/10.3390/math10091542

[25] B. W. Li, W. Wang, and J. K. Zhang, "Combined effects of magnetic field and thermal radiation on fluid flow

and heat transfer of mixed convection in a vertical cylindrical annulus," *J. Heat Transfer*, vol. 138, no. 6, p. 062501, 2016. https://doi.org/10.1115/1.4032609

[26] S. G. Bejawada and M. M. Nandeppanavar, "Effect of thermal radiation on magnetohydrodynamics heat transfer micropolar fluid flow over a vertical moving porous plate," *Exp. Comput. Multiph. Flow*, vol. 5, no. 2, pp. 149–158, 2022. https://doi.org/10.1007/s42757-021-0131-5

[27] K. Hosseinzadeh, M. Gholinia, B. Jafari, A. Ghanbarpour, H. Olfian, and D. D. Ganji, "Nonlinear thermal radiation and chemical reaction effects on Maxwell fluid flow with convectively heated plate in a porous medium," *Heat Transfer Asian Res.*, vol. 48, no. 2, pp. 744–759, 2018. https://doi.org/10.1002/htj.21404

[28] A. M. Megahed, "Williamson fluid flow due to a nonlinearly stretching sheet with viscous dissipation and thermal radiation," *J. Egypt. Math. Soc.*, vol. 27, no. 1, p. 12, 2019. https://doi.org/10.1186/s42787-019-0016-y

[29] H. Ragueb and K. Mansouri, "A numerical study of viscous dissipation effect on non-Newtonian fluid flow inside elliptical duct," *Energy Convers. Manage.*, vol. 68, pp. 124–132, 2013. https://doi.org/10.1016/j.enconman.2012.12.031

[30] F. S. Schranner, J. A. Domaradzki, S. Hickel, and N. A. Adams, "Assessing the numerical dissipation rate and viscosity in numerical simulations of fluid flows," *Comput. Fluids*, vol. 114, pp. 84–97, 2015. https://doi.org/10.1016/j.compfluid.2015.02.011

[31] D. Lelea and A. E. Cioabla, "The viscous dissipation effect on heat transfer and fluid flow in micro-tubes," *Int. Commun. Heat Mass Transfer*, vol. 37, no. 9, pp. 1208–1214, 2010. https://doi.org/10.1016/j.icheatmasstransfer.2010.06.030

[32] R. C. Bataller, "Viscoelastic fluid flow and heat transfer over a stretching sheet under the effects of a non-uniform heat source, viscous dissipation and thermal radiation," *Int. J. Heat Mass Transfer*, vol. 50, no. 15-16, pp. 3152–3162, 2007. https://doi.org/10.1016/j.ijheatmasstransfer.2007.01.003

[33] C. P. Tso, J. Sheela-Francisca, and Y. M. Hung, "Viscous dissipation effects of power-law fluid flow within parallel plates with constant heat fluxes," *J. Non-Newtonian Fluid Mech.*, vol. 165, no. 11-12, pp. 625–630, 2010. https://doi.org/10.1016/j.jnnfm.2010.02.023

[34] P. K. Dadheech, P. Agrawal, A. Sharma, K. S. Nisar, and S. D. Purohit, "Transportation of Al_2O_3-SiO_2-TiO_2 modified nanofluid over an exponentially stretching surface with inclined magnetohydrodynamic," *Therm. Sci.*, vol. 25, no. Spec. issue 2, pp. 279–285, 2021. https://doi.org/10.2298/TSCI21S2279D

[35] L. J. Crane, "Flow past a stretching plate," *Z. Angew. Math. Phys.*, vol. 21, no. 4, pp. 645–647, 1970. https://doi.org/10.1007/BF01587695

[36] M. Hamid, M. Usman, Z. Khan, R. Ahmad, and W. Wang, "Dual solutions and stability analysis of flow and heat transfer of Casson fluid over a stretching sheet," *Phys. Lett. A*, vol. 383, no. 20, pp. 2400–2408, 2019. https://doi.org/10.1016/j.physleta.2019.04.050

[37] J. Xiang, J. Liu, W. Yang, X. Wei, P. Li, Z. Chen, Y. Zheng, and J. Huang, "Development of novel thermal diode based on improved check valve and modified wick structure," *Int. J. Therm. Sci.*, vol. 200, p. 108977, 2024. https://doi.org/10.1016/j.ijthermalsci.2024.108977

[38] M. Shanmugam and L. S. Maganti, "Experimental investigation of microchannel heat sink performance under non-uniform heat load conditions with different flow configurations," *Int. J. Therm. Sci.*, vol. 203, p. 109128, 2024. https://doi.org/10.1016/j.ijthermalsci.2024.109128

[39] D. Agravat, S. K. Patel, and O. Alsalman, "Investigation of graphene-perovskite integration for enhanced absorption of solar thermal absorber for industrial heating applications," *Int. J. Therm. Sci.*, vol. 201, p. 109029, 2024. https://doi.org/10.1016/j.ijthermalsci.2024.109029

[40] M. Ullah, H. Fiaz, A. Abbas, K. Shaker, Y. Nawab, and M. Umair, "Thermal comfort and mechanical analysis of vigorous diamond and diaper weaves; warp, weft and balanced float fabrics with equal thread densities," *Int. J. Therm. Sci.*, vol. 204, p. 109235, 2024. https://doi.org/10.1016/j.ijthermalsci.2024.109235

[41] H. Flity, Y. Jannot, L. Terrei, P. Lardet, V. Schick, Z. Acem, and G. Parent, "Thermal conductivity parallel and perpendicular to fibers direction and heat capacity measurements of eight wood species up to 160 °C," *Int. J. Therm. Sci.*, vol. 195, p. 108661, 2024. https://doi.org/10.1016/j.ijthermalsci.2023.108661

[42] G. Bognár, "On similarity solutions of boundary layer problems with upstream moving wall in non-Newtonian power-law fluids," *IMA J. Appl. Math.*, vol. 77, no. 4, pp. 546–562, 2011. https://doi.org/10.1093/imamat/hxr033

[43] S. A. Lone, F. Ali, A. Saeed, and G. Bognár, "Irreversibility analysis with hybrid cross nanofluid of stagnation point and radiative flow (TiO_2 + CuO) based on engine oil past a stretchable sheet," *Heliyon*, vol. 9, no. 4, p. e15056, 2023. https://doi.org/10.1016/j.heliyon.2023.e15056

[44] I. F. Barna, G. Bognár, M. Guedda, L. Mátyás, and K. Hriczó, "Analytic self-similar solutions of the Kardar-Parisi-Zhang interface growing equation with various noise terms," *Math. Model. Anal.*, vol. 25, no. 2, pp. 241–256, 2020. https://doi.org/10.3846/mma.2020.10459

[45] M. Klazly and G. Bognár, "A novel empirical equation for the effective viscosity of nanofluids based on

theoretical and empirical results," *Int. Commun. Heat Mass Transfer*, vol. 135, p. 106054, 2022. https://doi.org/10.1016/j.icheatmasstransfer.2022.106054

[46] G. Bognár and K. Hriczó, "Ferrofluid flow in magnetic field above stretching sheet with suction and injection," *Math. Model. Anal.*, vol. 25, no. 3, pp. 461–472, 2020. https://doi.org/10.3846/mma.2020.10837

[47] W. K. Usafzai, E. H. Aly, M. M. Tharwat, and A. M. Mahros, "Modeling of micropolar nanofluid flow over flat surface with slip velocity and heat transfer: Exact multiple solutions," *Alex. Eng. J.*, vol. 75, pp. 313–323, 2023. https://doi.org/10.1016/j.aej.2023.06.004

[48] U. S. Mahabaleshwar, S. M. Sachhin, L. M. Pérez, and G. Lorenzini, "An effect of mass transpiration and Darcy–Brinkman model on Ostwald–de Waele Ternary nanofluid," *J. Eng. Thermophys.*, vol. 33, no. 3, pp. 547–565, 2024. https://doi.org/10.1134/S181023282403010X

[49] U. Mahabaleshwar, D. Basavaraja, S. Wang, G. Lorenzini, and E. Lorenzini, "Convection in a porous medium with variable internal heat source and variable gravity," *Int. J. Heat Mass Transfer*, vol. 111, pp. 651–656, 2017. https://doi.org/10.1016/j.ijheatmasstransfer.2017.04.030

[50] U. S. Mahabaleshwar, I. E. Sarris, A. A. Hill, G. Lorenzini, and I. Pop, "An MHD couple stress fluid due to a perforated sheet undergoing linear stretching with heat transfer," *Int. J. Heat Mass Transfer*, vol. 105, pp. 157–167, 2017. https://doi.org/10.1016/j.ijheatmasstransfer.2016.09.040

[51] U. Khan, A. Zaib, A. Ishak, N. C. Roy, S. A. Bakar, T. Muhammad, A. H. Abdel-Aty, and I. S. Yahia, "Exact solutions for MHD axisymmetric hybrid nanofluid flow and heat transfer over a permeable non-linear radially shrinking/stretching surface with mutual impacts of thermal radiation," *Eur. Phys. J. Spec. Top.*, vol. 231, no. 6, pp. 1195–1204, 2022. https://doi.org/10.1140/epjs/s11734-022-00529-2

[52] M. Hatami and D. D. Ganji, "Natural convection of sodium alginate (SA) non-Newtonian nanofluid flow between two vertical flat plates by analytical and numerical methods," *Case Stud. Therm. Eng.*, vol. 2, pp. 14–22, 2014. https://doi.org/10.1016/j.csite.2013.11.001

[53] A. S. Jenifer and P. Saikrishnan, "Mixed convective bi-component SiO_2-Al_2O_3/H_2O hybrid nanofluid flow over a sphere," *J. Therm. Anal. Calorim.*, vol. 148, no. 12, pp. 5603–5612, 2023. https://doi.org/10.1007/s10973-023-12131-2

[54] S. M. Sachhin, U. S. Mahabaleshwar, N. Swaminathan, L. M. Pérez, and J. Wang, "Thermal dynamics and magnetohydrodynamics in ferrofluidic wall jet flow: Entropy generation in heat and mass transfer," *J. Mol. Liq.*, vol. 427, p. 127449, 2025. https://doi.org/10.1016/j.molliq.2025.127449

Nomenclature

A	First order slip coefficient
A_1, A_2, A_3, A_4, A_5	Constants
Al_2O_3	Aluminium oxide
B	Second order slip coefficient
SiO_2	Silicon dioxide
TiO_2	Titanium dioxide
C_p	Specific heat
D	Mass flux
Da^{-1}	Inverse Darcy number
a	Stretching rate
c	Acceleration rate
B_0	Magnetic strength
b, l	Constants
Ec_1, Ec_2	Eckert numbers
K^*	Permeability of porous medium
M	Magnetic field parameter
Nr	Thermal radiation parameter
N_i	Heat source/sink parameter
Λ	Viscosity ratio
Pr	Prandtl number
Re_x	Reynolds number
q_r	Radiative heat flux
S	Mass suction/injection
d	Stretching/shrinking parameter
f	Velocity function
Q_0	Heat source/sink coefficient

T_w	Surface temperature
T_∞	Ambient temperature
T	Fluid temperature
u, v	Velocity components
u_w, v_w	Wall velocities
x, y	Coordinate axes

Greek symbols

β	Solution term
η	Similarity variable
ρ	Fluid density
ψ	Stream function
κ	Thermal conductivity
k^*	Absorption coefficient
μ	Dynamic viscosity
ν	Kinematic viscosity
σ	Electrical conductivity
σ^*	Stefan–Boltzmann constant
θ	PST temperature
φ	PHF temperature
ϕ	Nanoparticles volume fraction
ξ_1	First order velocity slip parameter
ξ_2	Second order velocity slip parameter

Subscripts

HNF	Hybrid nanofluid
B.Cs	Boundary conditions
PDE	Partial differential equation
ODE	Ordinary differential equation
MHD	Magnetohydrodynamics
PHF	Prescribed heat flux
PST	Prescribed surface temperature